Evidence of a room-temperature quantum spin Hall edge state in a higher-order topological insulator

Nana Shumiya[1,19], Md Shafayat Hossain[1,19 ✉], Jia-Xin Yin[1,19 ✉], Zhiwei Wang[2,3,19], Maksim Litskevich[1,19], Chiho Yoon[4,5,19], Yongkai Li[2,3], Ying Yang[2,3], Yu-Xiao Jiang[1], Guangming Cheng[6], Yen-Chuan Lin[7], Qi Zhang[1], Zi-Jia Cheng[1], Tyler A. Cochran[1], Daniel Multer[1], Xian P. Yang[1], Brian Casas[8], Tay-Rong Chang[9,10,11], Titus Neupert[12], Zhujun Yuan[13,14,15], Shuang Jia[13,14,15], Hsin Lin[16], Nan Yao[6], Luis Balicas[8], Fan Zhang[4], Yugui Yao[2,3] and M. Zahid Hasan[1,17,18 ✉]

Room-temperature realization of macroscopic quantum phases is one of the major pursuits in fundamental physics[1,2]. The quantum spin Hall phase[3–6] is a topological quantum phase that features a two-dimensional insulating bulk and a helical edge state. Here we use vector magnetic field and variable temperature based scanning tunnelling microscopy to provide micro-spectroscopic evidence for a room-temperature quantum spin Hall edge state on the surface of the higher-order topological insulator Bi_4Br_4. We find that the atomically resolved lattice exhibits a large insulating gap of over 200 meV, and an atomically sharp monolayer step edge hosts an in-gap gapless state, suggesting topological bulk–boundary correspondence. An external magnetic field can gap the edge state, consistent with the time-reversal symmetry protection inherent in the underlying band topology. We further identify the geometrical hybridization of such edge states, which not only supports the Z_2 topology of the quantum spin Hall state but also visualizes the building blocks of the higher-order topological insulator phase. Our results further encourage the exploration of high-temperature transport quantization of the putative topological phase reported here.

A topological insulator is a material that behaves as an insulator in its interior but whose surface contains protected conducting states[3,7–9]. A two-dimensional (2D) topological insulator features time-reversal symmetry-protected helical edge states residing in an insulating bulk gap (Fig. 1a shows both real-space and momentum-space pictures of a helical edge state) and accordingly exhibits the quantum spin Hall effect[4–6,10–13]. The helical edge state features dissipationless electron channels along the sample edges (Fig. 1a), which is of great interest in energy-saving technology and quantum information science. Equipped with high spatial

resolution, electronic detection and magnetic-field tunability, the state-of-the-art scanning tunnelling microscopy has been very powerful to discover and elucidate topological edge states in quantum materials[13–26]. Among topological insulator candidates, Bi_4Br_4 has a layered structure with van der Waals–like bonding, and has been proposed to feature a large insulating gap and weak interlayer coupling; thus, monolayer Bi_4Br_4 has the potential to realize a high-temperature quantum spin Hall state[27–32] in both freestanding[27] and bulk[32] environments. Although previous work using the angle-resolved photoemission technique[33] set out to resolve the topological boundary mode from crystalline steps, it remains elusive whether the observed boundary mode signal arises from the side surfaces or atomic step edges of the crystal. The magnetic-field response and temperature robustness of the predicted quantum spin Hall state are also largely unexplored, which will provide indispensable information for the underlying quantum topology and future applications of this quantum material. Therefore, a real-space experimental investigation of the nature of the edge state with atomic-layer spatial resolution, magnetic-field tunability and temperature control is highly desirable. In this work, we use vector field and variable temperature based scanning tunnelling microscopy to evidence and elucidate its insulating gap and topological edge state.

The crystal structure of α-Bi_4Br_4 is shown in Fig. 1b, which exhibits an interlayer stacking along the *c* axis and quasi-one-dimensional chains running along the *b* axis within each layer. Notably, two adjacent layers tilt towards different directions, as evidenced by our scanning transmission electron microscopy image visualizing the AB stacking (Fig. 1c). For our scanning tunnelling microscopy measurements, we cleave the single crystal in situ and measure at a temperature of 4.2 K, obtaining atomically clean surfaces (Fig. 1d). Clearly, the topographic image breaks mirror symmetry along the
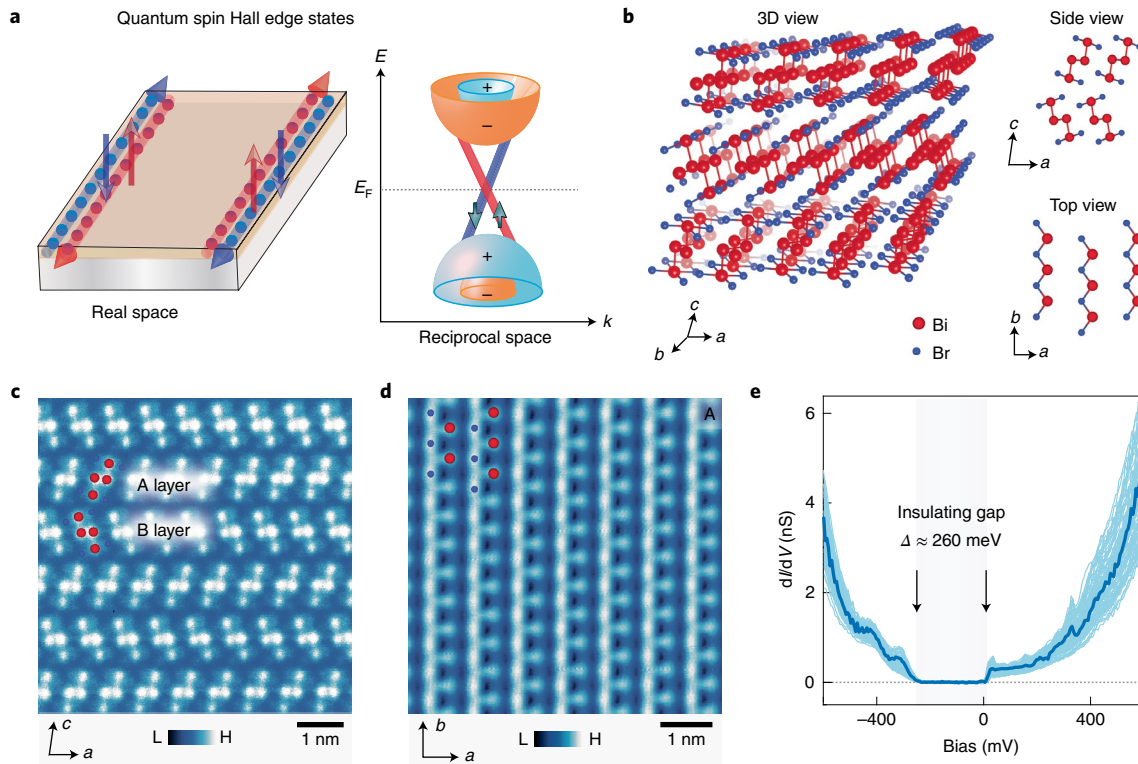
Fig. 1 | Observation of a large insulating energy gap. a, Schematic of the quantum spin Hall edge state: counterpropagating helical edge states with spin-up (red) and spin-down (blue) dissipationless channels in real space (left); the same topological edge states with red and blue bands (cartoon view) projected in the surface momentum space (right). The edge states originate from bulk band inversion, which is sketched by orange and light-blue bands. '+' and '−' denote the bulk bands with even and odd parities, respectively. **b**, Three-dimensional crystal structure, top view of monolayer (bottom right) and side view of the bulk (top right) α-Bi_4Br_4. **c**, Scanning transmission electron microscopy image from a lateral perspective, showing the atomic interlayer AB stacking. **d**, Atomically resolved scanning tunnelling microscopy image of the cleaving surface showing the type-A lattice. **e**, Tunnelling spectroscopy taken at 4.2 K, revealing an insulating gap. The light-blue curves are the differential spectra taken at different positions on the surface; the dark-blue curve denotes the average spectra.

a axis, and its symmetry-breaking direction allows us to determine this layer as the A layer (Fig. 1c). The determination of mirror symmetry breaking of the lattice is crucial for us to perform an analysis of the step edge geometry. The tunnelling differential conductance (dI/dV) that directly measures the local density of states (DOS) reveals a large insulating gap of $\Delta = 260$ meV on the atomic lattice (Fig. 1e). Such a large gap is consistent with the bulk insulating gap calculated from first-principles calculations[32] and observed by angle-resolved photoemission spectroscopy[33].

To further explore the topological nature of the insulating gap, we check the topological bulk–boundary correspondence (Fig. 2a). We perform the dI/dV spectroscopic maps at a monolayer step edge identified by a topographic image (Fig. 2a). As the electronic structure at the Fermi level is often regarded to be the most important for a quantum material, we focus on presenting the real-space differential conductance maps at the Fermi level. We find that the step edge exhibits pronounced edge states within the insulating gap (Fig. 2b, left, shows the spectroscopic imaging and Fig. 2d shows the tunnelling spectra). We note that although our tunnelling spectrum by its principle does not measure the absolute value of the local DOS per se, it unambiguously determines the evolution of gapped states into gapless states towards the edge. Figure 2b (left) shows the decay of the edge state on the crystal side of the step edge. Although the edge state decays more sharply on the vacuum side, it decays with a characteristic length of $r_0 \approx 2.1$ nm on the crystal side. The penetration depth of a topological boundary mode can be generically estimated[8] by $r_0 = 2\hbar v_F/\Delta$, where v_F is the bulk-avoided Fermi velocity. This allows us to further estimate the Fermi velocity to be 0.27 eV nm, which is of the same order of

magnitude as the one calculated by first-principles calculations[32] and determined by angle-resolved photoemission experiment[33]. The dI/dV spectrum taken at the step edge clearly shows the existence of the gapless in-gap state (Fig. 2d). At the Fermi energy, the in-gap state exhibits a dip feature. Such a zero-bias anomaly has been consistently reported in quantum spin Hall edge state systems[11,17–25,34], as a result of the Tomonaga–Luttinger liquid behaviour due to edge electron–electron interactions.

Furthermore, the quantum topology of the system has been proposed to be protected by the time-reversal symmetry[27,32], which can be broken by applying an external magnetic field. When we apply a strong magnetic field perpendicular to the *a*–*b* plane, we find that the in-gap state measured at the edge is substantially suppressed (Fig. 2c, $B = 4$ and 8 T), and an energy gap progressively develops for the edge state (Fig. 2e,f). The magnetic field essentially opens a gap at the edge-state Dirac point. The energy gap position (Fig. 2f) suggests that the Dirac point is slightly above the Fermi level. From our field-dependent data, we estimate the gap-opening rate of 3 meV T^{-1}, which amounts to a large *c*-axis Landé *g* factor of 53. This large *g* factor is likely due to the form and magnitude of spin–orbit coupling whose impact on the band structure is also substantial[32]. We note that for this material, the Dirac point energy and band dispersion of the edge state may be subject to band bending induced by the probe tip[35,36]. The bulk–boundary correspondence together with the response to the breaking of time-reversal symmetry demonstrated here provide experimental evidence for the topological nature of the system[27].

To further evidence the Z_2 topological nature of the monolayer step edge, we study their quantum hybridization. The hybridization
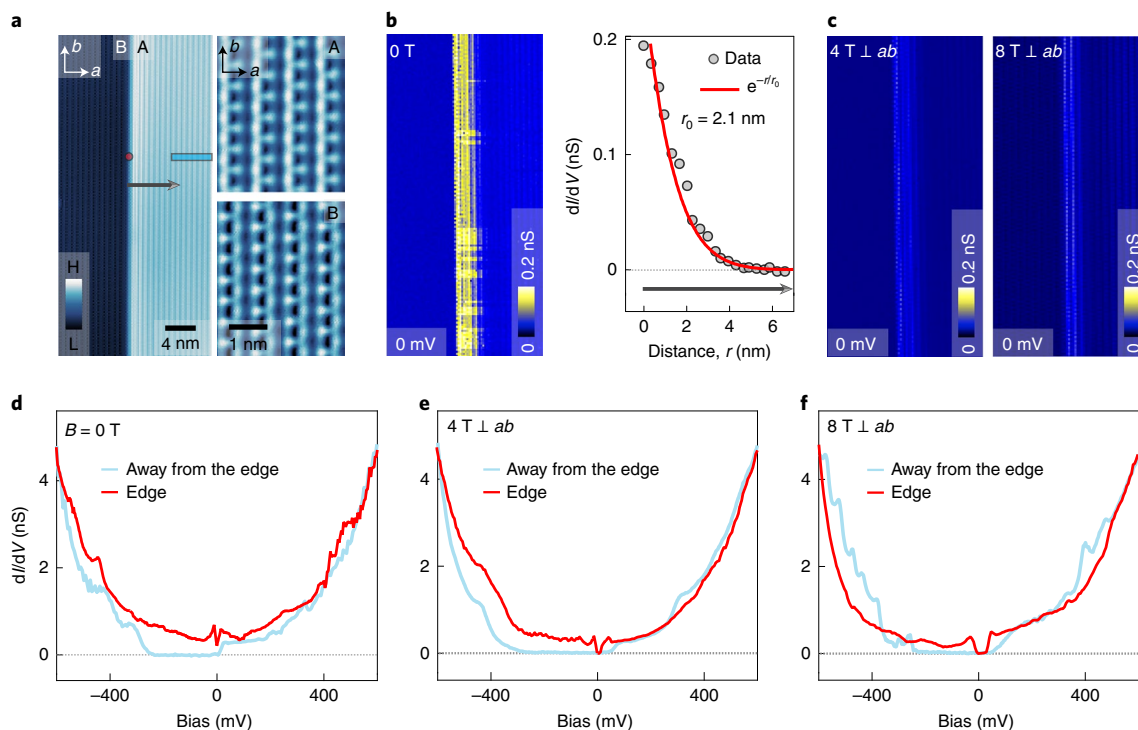
Fig. 2 | Evidence of a quantum spin Hall edge state. a, Topographic image of an atomically sharp monolayer AB step edge. An enlarged atomically resolved view of A and B surfaces are shown in the right panels. **b**, The dI/dV map taken at $B = 0\,T$ ($V = 0\,mV$) showing a pronounced in-gap edge state (left). Intensity distribution of differential conductance taken at $0\,mV$ away from the step edge (right) (the corresponding location is marked on the topographic image in **a** with a black line; the direction of the scan is marked with an arrow). The red curve shows the exponential fitting of the decay of the state away from the edge. **c**, The dI/dV maps taken at $B = 4$ and $8\,T$ ($V = 0\,mV$) shown using the same colour scale as in **b**. **d–f**, Differential spectra at $B = 0\,T$ (**d**), $4\,T$ (**e**) and $8\,T$ (**f**), further highlighting the effect of time-reversal symmetry breaking on the edge state. The red and blue curves denote the spectra taken at the edge and far away from the edge (locations marked in the topography image in **a**; blue curves are averaged over the marked region), respectively. The spectra at different magnetic fields are taken at the same locations, and using standard lock-in technique with a frequency of $977\,Hz$ and a junction setup of $V = -600\,mV$, $I = 0.5\,nA$ and a root mean square oscillation voltage of $1\,mV$. At $B = 4$ and $8\,T$, the edge state is clearly suppressed, and a gap gradually develops at the Fermi level as a function of the magnetic field.

of two Z_2 edge modes is destructive and opens an energy gap. Specific to this material, rooted in the fact that the inversion centre is in the monolayer instead of in the centre of a bilayer[32], the left and right AB bilayer edges have different geometries (Fig. 3a). On the left, the edges of the A and B layers have a facing angle larger than 180°, whereas on the right, the facing angle is smaller than 180°. This inversion asymmetry leads to stronger hybridization of the monolayer edge states on the right[32]. Similarly, for a BA bilayer, it can be inferred that the left side has stronger hybridization (not shown). Notably, this interlayer edge state hybridization has been pointed out as a key building block of the bulk higher-order topological insulator[37–40] that exhibits helical hinge states[32] (Fig. 3b). Figure 3c shows a case region containing a monolayer step edge as well as a left edge of the AB bilayer. The associated dI/dV mapping confirms the existence of in-gap edge states in both cases. To visualize the asymmetric hybridization of the edge states (Fig. 3a), we extensively scan the crystal to find an area containing both left and right AB bilayer step edges (Fig. 3d). The differential spectra taken at the two AB bilayer step edges (Fig. 3e) reveal their dramatically different behaviours. The in-gap state for the right AB bilayer edge is substantially suppressed compared with that on the left AB bilayer edge. The inversion asymmetry of the bilayer edge state is further visualized in Fig. 3f, which demonstrates the dI/dV maps of the same area as in Fig. 3d, taken at two representative energies within the insulating gap. It is shown that the edge state mainly shows up for the left AB bilayer edge, in agreement with the picture in Fig. 3a. The geometrical dependence of the bilayer step edge states not only supports the Z_2 topology of the potential quantum spin Hall

state within each monolayer but also demonstrates the building block of the bulk higher-order topological insulator.

Having evidenced an edge state at low temperature, we further explore its character by progressively increasing the temperature. In Fig. 4a, we show the dI/dV spectra of the lattice and monolayer step edge, taken at high temperatures of 100, 200 and 300 K. Similar to our dI/dV data at $T = 4.2\,K$, at all the three temperatures, both insulating gap and in-gap edge state persist. Although the insulating gap appears to shrink to $\sim$230 meV (by $\sim$10%) owing to thermal broadening and other factors, the Fermi level remains in the gap. The temperature robustness of the topological edge state is further demonstrated (Fig. 4b) where we show topographic images around a step edge and dI/dV maps of the same area, taken at zero energy for the different temperatures. In all the cases, the step edge exhibits a pronounced localized state. The presence of the topological edge state at room temperature is further substantiated in the dI/dV spectra (Fig. 4c) taken along a line perpendicular to the edge shown in Fig. 4b (top). At and very near the position of the edge, the in-gap edge states emerge, whereas on the surface away from the edge, the spectra are gapped near the Fermi energy. Our evidence for a quantum spin Hall edge state and the insulating gap at the Fermi level at room temperature microscopically demonstrates the building block of a higher-order topological insulator. In magnetically doped topological insulators, the topological gap is spatially inhomogeneous, which severely limits the lifetime of the chiral edge states[41]. In striking contrast, the large bulk insulating gap in this stoichiometric material is shown to be rather homogeneous in our study, and the lifetime of
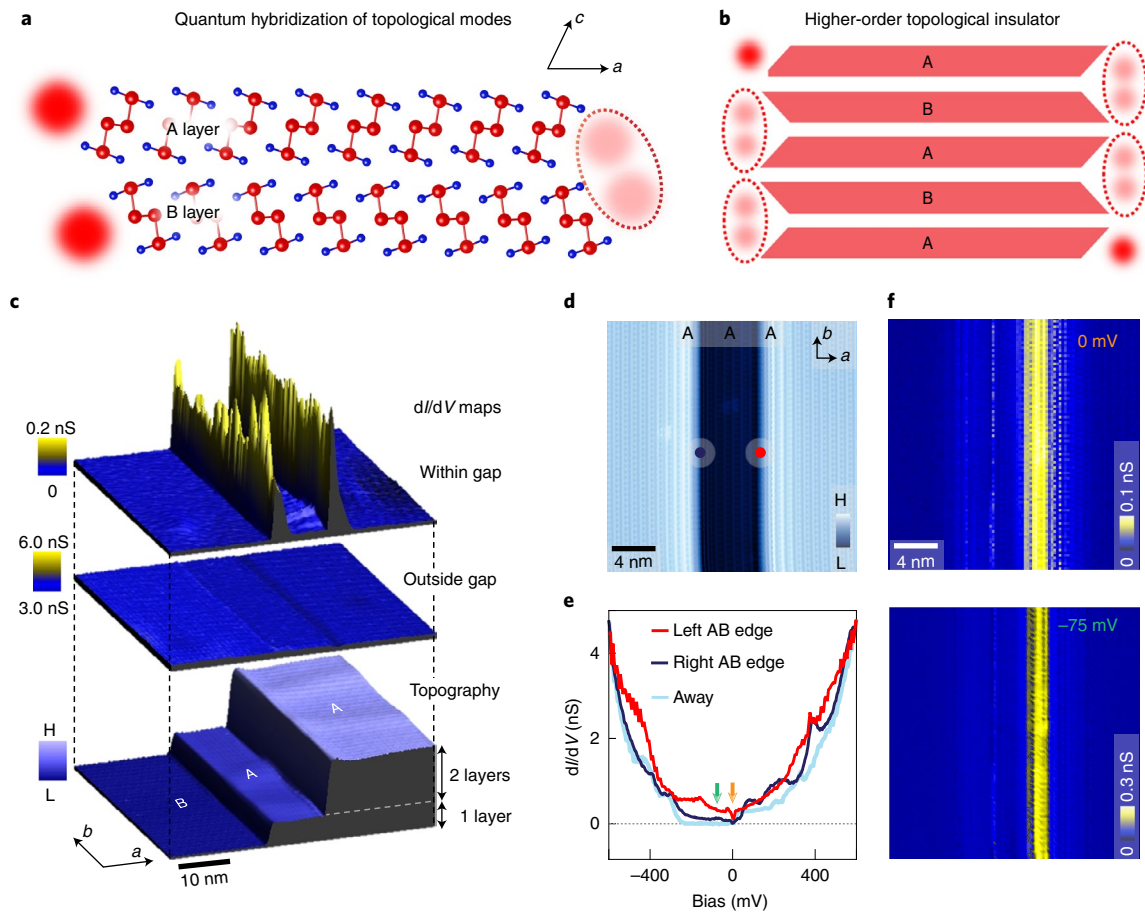
Fig. 3 | Geometrical hybridization of edge states. a, Side view of an AB bilayer. Edges of the A and B layers having a facing angle larger than 180° (left) and facing angle smaller than 180° (right). This geometrical difference leads to stronger hybridization of the two monolayer edge states (red spheres) on the right. The hybridization of the edge state is destructive, as illustrated by the lighter colour of the edge states (red spheres). **b**, Construction of a higher-order topological insulator based on the hybridization mechanism in **a**. The higher-order topological insulator in this case exhibits two hinge modes on the top-left and bottom-right corners. **c**, Spectroscopic imaging of the crystalline steps. The bottom panel shows the topographic image of the two step edges. The middle panel shows the corresponding differential conductance map obtained at energy outside the insulating gap. The top layer shows the corresponding differential conductance map obtained at energy inside the insulating gap, revealing pronounced edge states. **d**, Topographic image of two adjacent bilayer atomic step edges forming a trench. **e**, Differential spectra taken at the left AB bilayer step edge (red), right AB bilayer step edge (violet) and away from the edges (blue), revealing striking differences between the two step edges. The violet and red dots in **d** denote the respective positions on the left and right AB edges where the differential spectra are taken. The left AB edge exhibits a pronounced in-gap state, whereas on the right AB edge, the DOS at the bulk gap is largely suppressed. **f**, Differential conductance map, taken at $V = 0$ and -75 mV (marked with colour-coded arrows in the differential spectra in **e**), shown in two layers, namely, $V = 0$ and -75 mV, both of which are inside the insulating gap.

helical edge states was recently reported to be ultralong[42]. We anticipate a transport measurement of the putative high-temperature quantum spin Hall effect of this material in the near future. The evidence provided here for room-temperature quantum spin Hall state suggests that it does not require extreme conditions, including giant pressure[2] or high magnetic field[1]; therefore, it holds great potential for next-generation quantum technologies.

Online content

Any methods, additional references, Nature Research reporting summaries, source data, extended data, supplementary information, acknowledgements, peer review information; details of author contributions and competing interests; and statements of data and code availability are available at https://doi.org/10.1038/s41563-022-01304-3.

References

1. Novoselov, K. S. et al. Room-temperature quantum Hall effect in graphene. *Science* **315**, 1379 (2007).
2. Snider, E. et al. Room-temperature superconductivity in a carbonaceous sulfur hydride. *Nature* **586**, 373–377 (2020).
3. Hasan, M. Z. & Kane, C. L. Colloquium: topological insulators. *Rev. Mod. Phys.* **82**, 3045 (2010).
4. Kane, C. L. & Mele, E. J. Z_2 topological order and the quantum spin Hall effect. *Phys. Rev. Lett.* **95**, 146802 (2005).
5. Bernevig, B. A. & Zhang, S.-C. Quantum spin Hall effect. *Phys. Rev. Lett.* **96**, 106802 (2006).
6. König, M. et al. Quantum spin Hall insulator state in HgTe quantum wells. *Science* **318**, 766–770 (2007).
7. Qi, X.-L. & Zhang, S.-C. Topological insulators and superconductors. *Rev. Mod. Phys.* **83**, 1057 (2011).
8. Zhang, F., Kane, C. L. & Mele, E. J. Surface states of topological insulators. *Phys. Rev. B* **86**, 081303(R) (2012).
9. Bernevig, B. A. *Topological Insulators and Topological Superconductors* (Princeton Univ. Press, 2013).
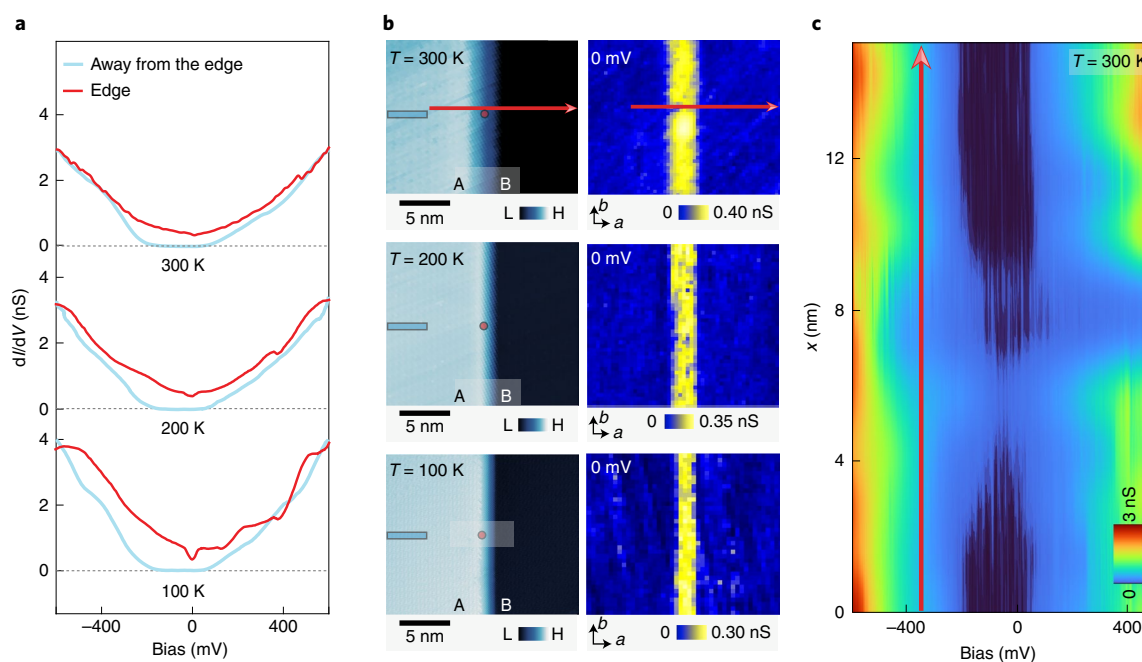10. Kane, C. L. & Mele, E. J. Quantum spin Hall effect in graphene. *Phys. Rev. Lett.* **95**, 226801 (2005).

Fig. 4 | Room-temperature edge state. a, Temperature-dependent differential spectra taken on the surface and edge, denoted with blue and red curves (locations marked in the corresponding topography images in **b**; blue curves are averaged over the blue-marked regions), respectively. The spectra are offset for clarity for different temperatures. **b**, Topography and corresponding differential conductance maps taken on a monolayer step edge at $T = 300$, 200 and 100 K ($V = 0$ mV), capturing the temperature robustness of the edge states. **c**, Intensity plot of a series of line spectra at $T = 300$ K, taken along the a-axis direction (marked on the corresponding topographic image in **b** with a red line; the direction of the scan is marked with an arrow), reveals the presence of a gapless edge state at room temperature.

11. Reis, F. et al. Bismuthene on a SiC substrate: a candidate for a high-temperature quantum spin Hall material. *Science* **357**, 287–290 (2017).
12. Wu, S. et al. Observation of the quantum spin Hall effect up to 100 Kelvin in a monolayer crystal. *Science* **359**, 76–79 (2018).
13. Tang, S. et al. Quantum spin Hall state in monolayer 1T′-WTe₂. *Nat. Phys.* **13**, 683–687 (2017).
14. Yin, J.-X., Pan, S. H. & Hasan, M. Z. Probing topological quantum matter with scanning tunnelling microscopy. *Nat. Rev. Phys.* **3**, 249–263 (2021).
15. Yang, F. et al. Spatial and energy distribution of topological edge states in single Bi(111) bilayer. *Phys. Rev. Lett.* **109**, 016801 (2012).
16. Drozdov, I. K. et al. One-dimensional topological edge states of bismuth bilayers. *Nat. Phys.* **10**, 664–669 (2014).
17. Pauly, C. et al. Subnanometre-wide electron channels protected by topology. *Nat. Phys.* **11**, 338–343 (2015).
18. Wu, R. et al. Evidence for topological edge states in a large energy gap near the step edges on the surface of ZrTe₅. *Phys. Rev. X* **6**, 021017 (2016).
19. Li, X.-B. et al. Experimental observation of topological edge states at the surface step edge of the topological insulator ZrTe₅. *Phys. Rev. Lett.* **116**, 176803 (2016).
20. Wang, Z. et al. Topological edge states in a high-temperature superconductor FeSe/SrTiO₃(001) film. *Nat. Mater.* **15**, 968–973 (2016).
21. Sessi, P. et al. Robust spin-polarized midgap states at step edges of topological crystalline insulators. *Science* **354**, 1269–1273 (2016).
22. Peng, L. et al. Observation of topological states residing at step edges of WTe₂. *Nat. Commun.* **8**, 659 (2017).
23. Liu, S. et al. Experimental observation of conductive edge states in weak topological insulator candidate HfTe₅. *APL Mater.* **6**, 121111 (2018).
24. Ugeda, M. M. et al. Observation of topologically protected states at crystalline phase boundaries in single-layer WSe₂. *Nat. Commun.* **9**, 3401 (2018).
25. Liu, R. Z. et al. Experimental observations indicating the topological nature of the edge states on HfTe₅. *Chinese Phys. Lett.* **36**, 117301 (2019).
26. Yin, J. X. et al. Quantum-limit Chern topological magnetism in TbMn₆Sn₆. *Nature* **583**, 533–536 (2020).
27. Zhou, J.-J., Feng, W., Liu, C.-C., Guan, S. & Yao, Y. Large-gap quantum spin Hall insulator in single layer bismuth monobromide Bi₄Br₄. *Nano Lett.* **14**, 4767–4771 (2014).
28. Zhou, J.-J., Feng, W., Liu, G.-B. & Yao, Y. Topological edge states in single- and multi-layer Bi₄Br₄. *New J. Phys.* **17**, 015004 (2015).
29. Liu, C.-C., Zhou, J.-J., Yao, Y. & Zhang, F. Weak topological insulators and composite Weyl semimetals: β-Bi₄X₄ (X = Br, I). *Phys. Rev. Lett.* **116**, 066801 (2016).
30. Hsu, C.-H. et al. Purely rotational symmetry-protected topological crystalline insulator α-Bi₄Br₄. *2D Mater.* **6**, 031004 (2019).
31. Li, X. et al. Pressure-induced phase transitions and superconductivity in a quasi–1-dimensional topological crystalline isulator α-Bi₄Br₄. *Proc. Natl Acad. Sci. USA* **116**, 17696–17700 (2019).
32. Yoon, C., Liu, C.-C., Min, H. & Zhang F. Quasi-one-dimensional higher-order topological insulators. Preprint at https://arxiv.org/abs/2005.14710 (2020).
33. Noguchi, R. et al. Evidence for a higher-order topological insulator in a three-dimensional material built from van der Waals stacking of bismuth-halide chains. *Nat. Mater.* **20**, 473–479 (2021).
34. Stühler, R. et al. Tomonaga–Luttinger liquid in the edge channels of a quantum spin Hall insulator. *Nat. Phys.* **16**, 47–51 (2020).
35. Morgenstern, M. et al. Low temperature scanning tunneling spectroscopy on InAs(110). *J. Electron Spectrosc. Relat. Phenom.* **109**, 127–145 (2000).
36. Cheng, P. et al. Landau quantization of topological surface states in Bi₂Se₃. *Phys. Rev. Lett.* **105**, 076801 (2010).
37. Zhang, F., Kane, C. L. & Mele, E. J. Surface state magnetization and chiral edge states on topological insulators. *Phys. Rev. Lett.* **110**, 046404 (2013).
38. Schindler, F. et al. Higher-order topological insulators. *Sci. Adv.* **4**, eaat0346 (2018).
39. Schindler, F. et al. Higher-order topology in bismuth. *Nat. Phys.* **14**, 918–924 (2018).
40. Langbehn, J., Peng, Y., Trifunovic, L., von Oppen, F. & Brouwer, P. W. Reflection-symmetric second-order topological insulators and superconductors. *Phys. Rev. Lett.* **119**, 246401 (2017).
41. Lee, I. et al. Imaging Dirac-mass disorder from magnetic dopant atoms in the ferromagnetic topological insulator Crₓ(Bi₀.₁Sb₀.₉)₂₋ₓTe₃. *Proc. Natl Acad. Sci. USA* **112**, 1316–1321 (2015).
42. Mao, P. et al. Ultralong carrier lifetime of topological edge states in α-Bi₄Br₄. Preprint at https://arxiv.org/abs/2007.00264 (2020).

Methods

Crystal growth. High-quality single crystals of α-Bi$_4$Br$_4$ were grown by a self-flux method. High-purity BiBr$_3$ powder (4 N) and Bi shot (6 N) were mixed in a molar ratio of 1:16 and then sealed in an evacuated quartz tube. The tube was put into a muffle furnace and slowly heated to 500 °C, at which it was held for 24 h. After that, it was cooled to 320 °C at the rate of 5 °C h^{-1} and subsequently to 275 °C at the rate of 2 °C h^{-1}. Finally, needle-shaped Bi$_4$Br$_4$ single crystals were obtained after the Bi flux was removed via centrifugation. To obtain high-quality crystals, we performed surface-cleaning procedures to remove the oxide layers formed in air on the raw shots of Bi, that is, Bi shots were sealed in a quartz tube filled with 0.8 atm. hydrogen and then annealed at 240 °C for 12 h.

Scanning tunnelling microscopy. Single crystals were mechanically cleaved in situ at 77 K in ultrahigh vacuum conditions and then immediately inserted into the microscope head, already at the base temperature of ^{4}He (4.2 K). More than 30 single crystals have been cleaved for this study. For each cleaved crystal, we explored surface areas over 5 μm × 5 μm to search for atomic flat surfaces. Topographic images in this work were taken with the tunnelling junction setup of $V = -600$ mV and $I = 0.05$ nA in the constant current mode. Tunnelling conductance spectra were obtained with a commercial Ir/Pt tip using standard lock-in amplifier techniques with a lock-in frequency of 977 Hz and a junction setup of $V = -600$ mV, $I = 0.5$ nA and a root mean square oscillation voltage of 1 mV. Tunnelling conductance maps were obtained with a junction setup of $V = -600$ mV, $I = 0.3$ nA and a root mean square oscillation voltage of 10 mV. The magnetic field was applied with a zero-field cooling method. For the field-dependent tunnelling conductance map, we first withdrew the tip away from the sample, and then slowly ramped the field to the desired field. Then, we reapproached the tip to the sample, found the same atomic area and then performed spectroscopic mapping at this magnetic field. For variable temperature measurement, we first withdrew the tip from the sample, and then raised the temperature and stabilized the temperature for 12 h, after which we reapproached the tip to the sample to perform tunnelling experiments.

Extended scanning tunnelling microscopy data. Figure 1e shows certain spreading of the tunnelling spectra at higher energies. As shown in Extended Data Fig. 1, both dI/dV map and spectra show a detectable intraunit cell variation, particularly at high energies. A similar behaviour is observed in other quantum materials whose surfaces are composed of different atoms. We further show extended dI/dV maps (Extended Data Fig. 2) with $V = 0$ mV (at Fermi energy), $V = -75$ mV (near the middle of the bulk insulating gap) and $V = -600$ mV (outside the insulating energy gap). For a one-dimensional helical edge state, the magnetic field along its spin direction only shifts the Dirac-point momentum, whereas the magnetic field in the perpendicular direction can induce a Zeeman gap[3]. Our 1 T in-plane magnetic-field data are consistent with this picture (Extended Data Fig. 3). We show a high-resolution image of the monolayer step edge in Extended Data Fig. 4. In comparison with the image far from the step edges, we show that there is no detectable change in the inter-stripe distance near the step edge. The step height from the topographic image enhances 5% at the position of the step edge compared with that away from the step edge. As the topographic image convolutes the atomic structure and integrated DOS, this enhancement is likely due to the contribution from the emerging step edge states. In Extended Data Fig. 5, we show tunnelling spectroscopy on both left and right monolayer step edges, and both data reveal gapless edge states. This observation is different from the bilayer step edge, and supports the quantum spin Hall state nature of the monolayer step edge state. Through our systematic search for higher step edge layers, we observe a four-layer step edge (Extended Data Fig. 6). At the edge, we observe gapless tunnelling data, which serves as a candidate for a gapless hinge-state signal. Finally, we show the individual dI/dV spectrum taken across a monolayer step edge at 300 K (Extended Data Fig. 7).

Extended theoretical elaboration. Informed by the bulk crystalline structure of Bi$_4$Br$_4$, first-principles calculations were performed with the Vienna ab initio simulation package code[43,44] to obtain the electronic band structures and analyse the topological character of the bands. To obtain more accurate information on bandgaps and band inversions, the Heyd–Scuseria–Ernzerhof hybrid functional method[45] was applied. The wannier90 code[46] was employed to construct the maximally localized Wannier functions for the p orbitals of Bi and Br, which were used to build an ab initio tight-binding model[32]. The band structures of monolayer, few-layers, step edges, top surface, side surfaces and bulk were calculated through this model.

By using this ab initio model, the one-layer-step-edge-projected band structure can be obtained in the bulk environment. In Extended Data Fig. 8, it is clear that the helical edge state along the chain direction (**b**) is present in a 270 meV gap. In the bulk, the Dirac velocity in the **a** direction is 0.2 eV nm, as estimated from the low-energy bulk bands, consistent with that evaluated from our experiment (discussed earlier). The linear edge state spectrum results in a constant DOS inversely proportional to the Fermi velocity. The constant DOS can be probed via the tunnelling conductance in the ideal single-particle scenario. However, fluctuations can arise due to the presence of electron–electron interactions,

electron–phonon couplings, impurities, lattice defects and so on. In particular, the presence of electron–electron interactions gives rise to Luttinger liquid behaviour, which yields a zero-bias dip in the tunnelling conductance at the Fermi energy.

As a higher-order topological insulator, it has been revealed that Bi$_4$Br$_4$ has a hinge-state profile depending on how its surfaces are terminated[32]. For a sample with perfectly uniform cuts at the (001), (00–1), (100) and (–100) surfaces, there is always one hinge at the top surface and one hinge at the bottom surface that host a helical hinge state. For an even-layer system, due to inversion asymmetry, such two special hinges are located on the same side surface, either the (100) or (–100) surface, as exemplified by the twenty-layer case (Extended Data Fig. 9a,c). The orange bands are the gapped (100) and (–100) side surface states, whereas the red bands are two helical hinge states localized at the two hinges of the (100) side surface. This feature is even robust in the thinnest limit—the bilayer case (Extended Data Fig. 9b,c).

Because the inversion centre is in the monolayer, the interlayer couplings are oppositely dimerized at the (100) and (–100) side surfaces. It follows that for a bilayer, the two helical edge states of the two constituent monolayers are coupled relatively stronger at one side whereas relatively weaker at the other side. The stronger coupling produces an edge state gap, whereas the weaker coupling, which turns out to be negligibly small, has little impact on the gapless edge states. These results for the bilayer case can be confirmed by calculations (Extended Data Fig. 9b,c). In the thick limit, nevertheless, the nearly gapless edge states at one side evolve into the protected gapless hinge states, whereas the strongly gapped edge states at the other side evolve into the gapped side surface states, as exemplified by the twenty-layer case (Extended Data Fig. 9a,c).

The first-principles calculation shown in Extended Data Fig. 9b suggests that the hybridization gap for the right edge state of the AB bilayer is around 25 meV. This is of the same order as the energy range of the full suppression of the tunnelling DOS near the Dirac point that is accidentally around the Fermi level. Beyond this energy range, one possible explanation for the reduction in tunnelling DOS is the tunnelling geometry of the right edge. Figure 3d shows the topographic image of two adjacent bilayer step edges forming a trench. In the real-space picture, the hybridization of the two right edge states produces hybridized orbitals that locate deeper into the trench. This orbital geometry naturally reduces the tunnelling probability to the tip, compared with a monolayer edge state or the left edge state of an AB bilayer. On the other hand, the tunnelling probability from the projected bulk states may be less affected by the edge geometry. Thus, the tunnelling signal at the right edge of the AB bilayer, which contains contributions from both projected bulk states and edge states, shows a full suppression of DOS in the small-energy range of the hybridization gap and a partial reduction in the tunnelling DOS elsewhere.

Finally, we discuss the magnetic-field effect on the monolayer helical edge state. The gapless nature of the helical edge state, that is, Kramers degeneracy at the Dirac point, is protected by time-reversal symmetry. When time-reversal symmetry is broken, for example, by applying a magnetic field, a Zeeman energy gap may be opened at the Dirac point[3]. Consider a simplified model Hamiltonian for the helical edge state: $H_0 = v\hbar k_y \sigma_y$, where σ_i ($i = x, y, z$) are Pauli matrices, v is the Dirac velocity and $\hbar$ is the Planck constant. The corresponding dispersions are $E_\pm = \pm v\hbar k_y$, and the two bands linearly cross at the Dirac point at $k_y = 0$. When the magnetic field is applied along the y axis, the resulting Zeeman term can be modelled as $H_\parallel = \alpha_y B_y \sigma_y$, where α_i ($i = x, y, z$) are coefficients related to the Landé g factor. In this case, the dispersions become $E_\pm = \pm v\hbar(k_y + \alpha_y B_y / v\hbar)$, that is, the band-crossing point is shifted along the k_y axis. When the magnetic field is applied along the z axis, the resulting Zeeman term can be modelled as $H_\perp = \alpha_z B_z \sigma_z$. In this case, the dispersions become $E_\pm = \pm(v^2\hbar^2 k_y^2 + \alpha_z^2 B_z^2)^{1/2}$, that is, the Dirac point is gapped. Similarly, when the magnetic field is applied along the x axis, the Dirac spectrum is similarly gapped.

Extended discussion on the band topology of Bi$_4$Br$_4$. For a (001) monolayer, it is a standard 2D Z_2 topological insulator with a helical edge state protected by time-reversal symmetry[27]. Since this 2D band topology has been well discussed earlier, below we elaborate the three-dimensional (3D) band topology of bulk Bi$_4$Br$_4$. In short, there are two types of topological boundary state known for this time-reversal invariant (that is, non-magnetic) spin–orbit-coupled bulk material: (1) higher-order hinge states and (2) surface Dirac cones.

(1) The higher-order band topology of 3D Bi$_4$Br$_4$ is protected by time-reversal and inversion symmetries. The resulting symmetry indicators for Bi$_4$Br$_4$ are $Z_{2,2,2,4} = \{0,0,0,2\}$ (ref. [30]). This means that the material is neither a strong nor a weak topological insulator. Rather, it features multiple band inversions in the bulk and a single protected helical hinge state on an inversion-symmetric path on the surface of any inversion-symmetric crystal. The hinges that feature this state exactly depend on the surface termination and cannot be predicted from the bulk electronic structure and its topological invariants[32]. Moreover, the helical hinge state can be protected by time-reversal symmetry alone, indicating that the hinge states can survive under weak inversion-symmetry breaking and in crystals with inversion-asymmetric terminations[32].

(2) Furthermore, 3D Bi$_4$Br$_4$ has a non-trivial Z_2 topological invariant protected by the C_2 rotation symmetry around the [010] axis, which is the atomic chain

direction. This features single band inversion in each of the two C_2-invariant subspaces[30]. It guarantees the existence of two gapless Dirac cones on any surface that preserves the C_2 rotation symmetry, that is, the (010) and (0−10) surfaces. When the C_2 rotation symmetry is broken at these surfaces, the surface states become gapped[32].

Therefore, an inversion- and C_2-symmetric rod-like crystal with two capping surfaces normal to the [010] direction would feature both helical hinge states along the [010] direction and gapless Dirac cones at the (010) and (0−10) surfaces (Extended Data Fig. 10). Such geometry shows that the two topological invariants are not completely independent: if a capping surface was not gapless, there is no possibility to connect the hinge states in a way that preserves the C_2 symmetry, given that the hinge states need to form a singly connected loop due to the spectral flow carried by them. Moreover, when the C_2 rotation symmetry is broken at the capping surfaces, the surface states become gapped, and their 'residue' forms the gapless hinge states connecting the original hinge states (Extended Data Fig. 10).

In our experiment, we do not probe the (010) surface. In general, it would be challenging to probe this surface, as a crystal termination perpendicular to the atomic chains does not naturally form a clean surface and because most probably the C_2 symmetry is unavoidably broken there. Thus, the (001) and (100) surfaces (as part of the step edge) that we probe do not carry any gapless surface states. This enables us to measure only the gapless hinge states in the bulk gap.

Data availability

The data that support the findings of this study are available from the corresponding authors upon reasonable request.

References

43. Kresse, G. & Furthmüller, J. Efficient iterative schemes for ab initio total-energy calculations using a plane-wave basis set. *Phys. Rev. B* **54**, 11169 (1996).
44. Perdew, J. P., Burke, K. & Ernzerhof, M. Generalized gradient approximation made simple. *Phys. Rev. Lett.* **77**, 3865 (1996).
45. Heyd, J., Scuseria, G. E. & Ernzerhof, M. J. Hybrid functionals based on a screened Coulomb potential. *Chem. Phys.* **118**, 8207–8215 (2003).
46. Mostofi, A. et al. wannier90: a tool for obtaining maximally-localised Wannier functions. *Comput. Phys. Commun.* **178**, 685–699 (2008).

Acknowledgements

Author contributions

STM experiments were performed by N.S., M.S.H., Y.-X.J. and M.L. in consultation with J.-X.Y. and M.Z.H. Crystal growth was carried out by Z.W., Y.L., Y.Yang, Z.Y. and S.J. Transmission electron microscopy measurements were performed by G.C. and N.Y. Theoretical calculations regarding the higher-order band topology were mainly carried out by C.Y. under the supervision of F.Z., in consultation with M.S.H., J.X.Y., Y.C.L., T.R.C., T.N., Y.Yao and M.Z.H. Figure development and writing of the paper were undertaken by N.S., M.S.H., J.-X.Y., F.Z. and M.Z.H. M.Z.H. supervised the project. All the authors discussed the results, interpretation and conclusion.

Competing interests

The authors declare no competing interests.

Additional information

Extended data is available for this paper at https://doi.org/10.1038/s41563-022-01304-3.

Correspondence and requests for materials should be addressed to Md Shafayat Hossain, Jia-Xin Yin or M. Zahid Hasan.

Peer review information *Nature Materials* thanks Liang Fu and the other, anonymous, reviewer(s) for their contribution to the peer review of this work.

Reprints and permissions information is available at www.nature.com/reprints.
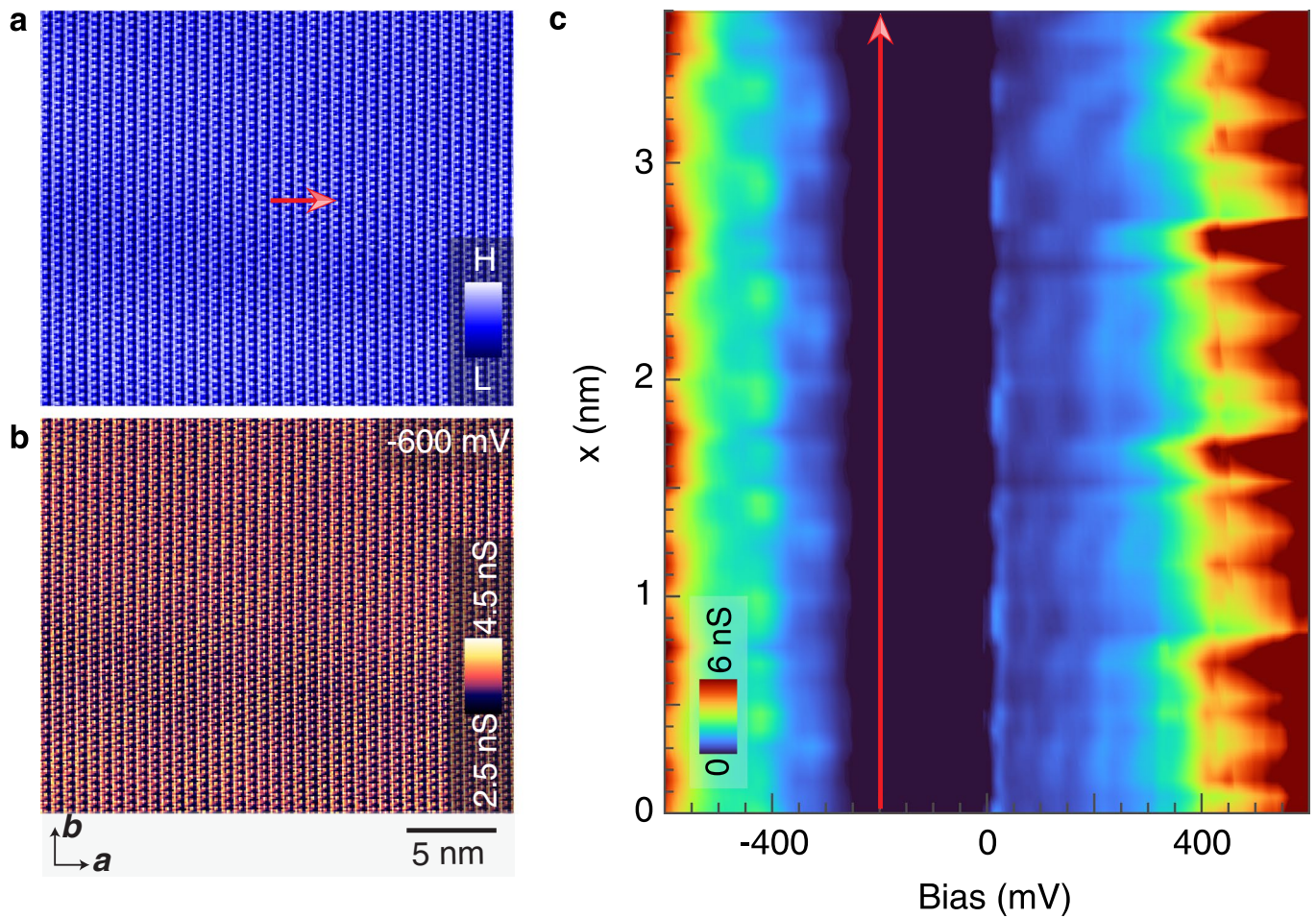
Extended Data Fig. 1 | Intra-unit cell modulation of differential conductance. a, Topography image of a clean region. b, Corresponding dI/dV map taken at V = 600 mV. c, Intensity plot of the dI/dV spectrum taken along the line in a.
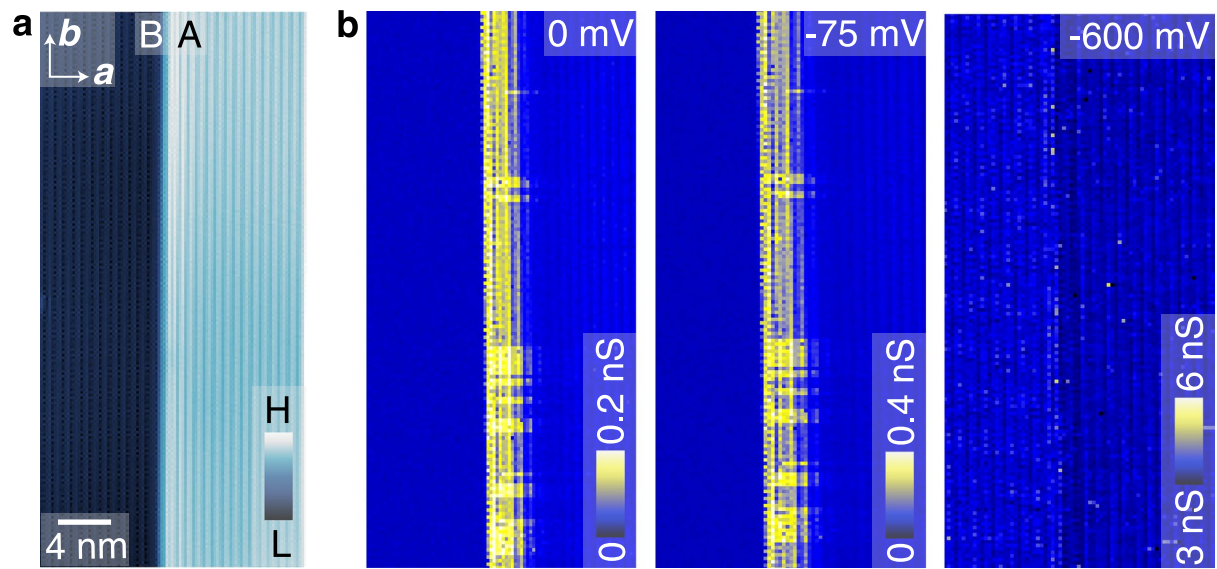
Extended Data Fig. 2 | Bias dependence of the monolayer edge state. a, Topographic image of an monolayer step edge. b, corresponding dI/dV maps, taken at V = 0 mV, -75mV, and -600mV.
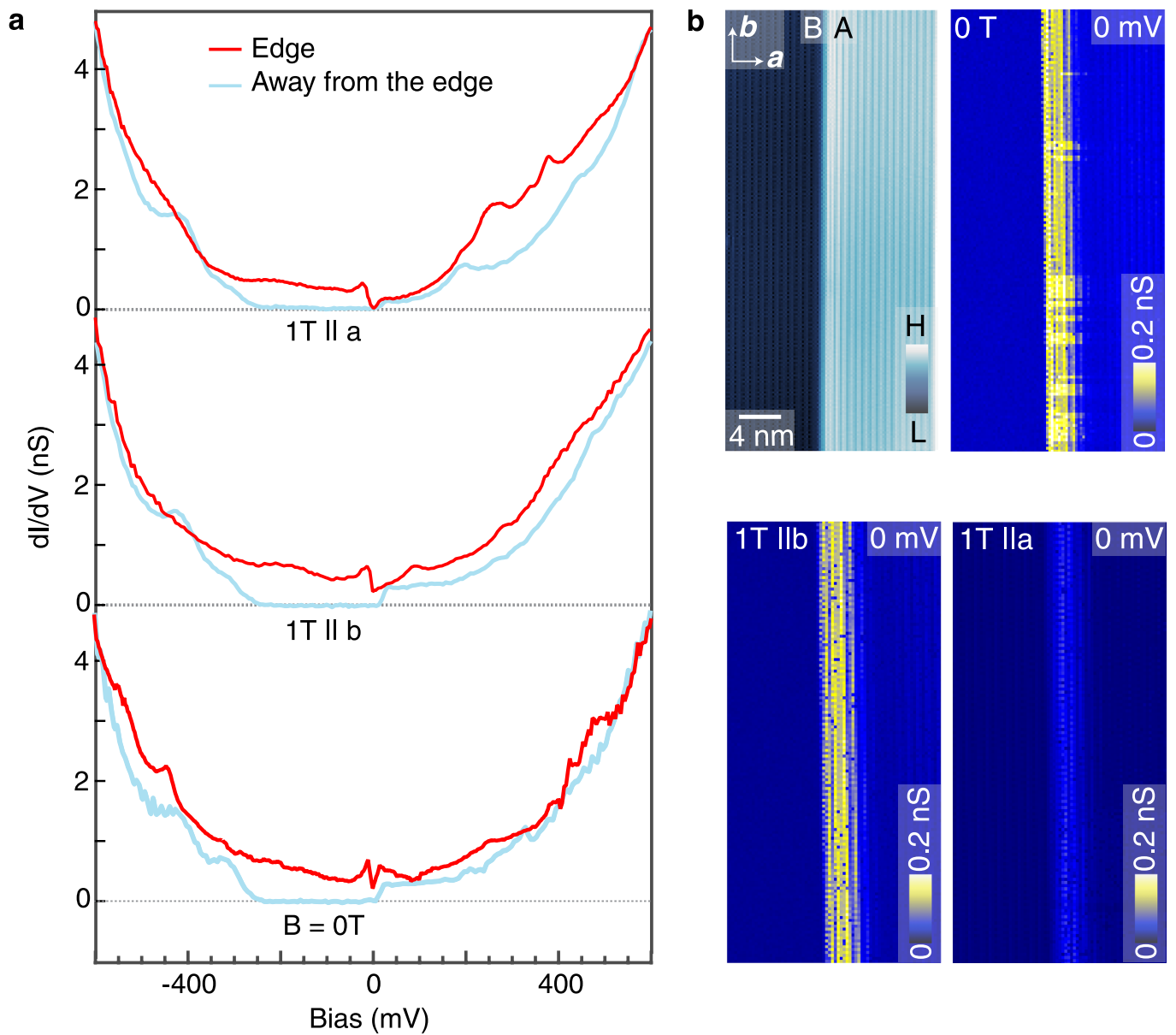
Extended Data Fig. 3 | Anisotropic in-plane magnetic field response of the edge state. a, Field dependent differential spectra taken on the edge and away from the edge, denoted with red and blue curves, respectively. Spectra are offset for clarity. b, Topography and the corresponding field dependent dI/dV maps (shown by using the same color scale) further elucidating the anisotropic in-plane magnetic field response of the edge state.
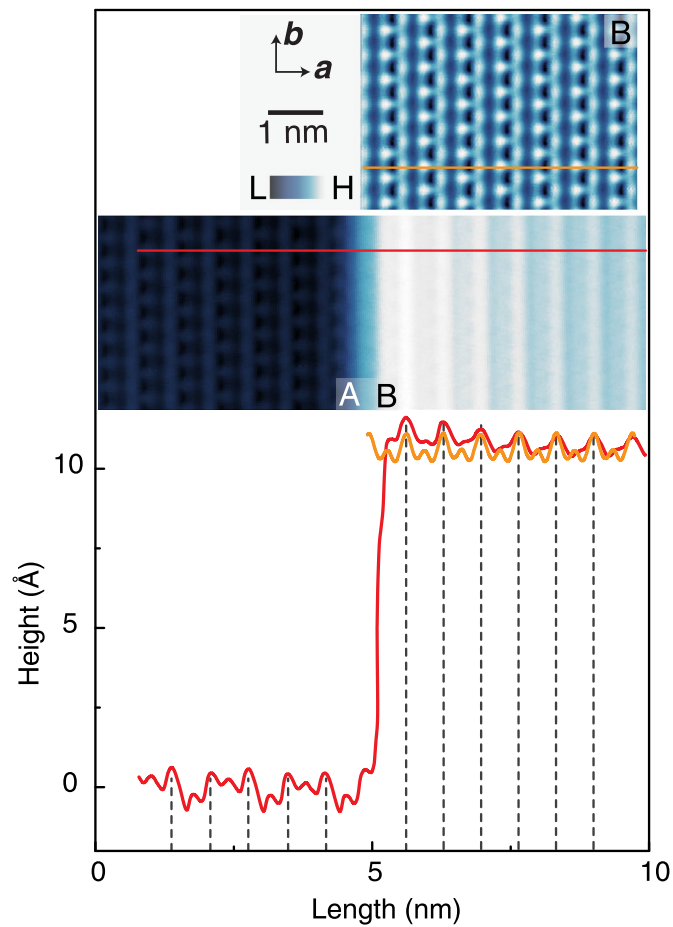
Extended Data Fig. 4 | High-resolution imaging of the monolayer step edge. We show the height profile across a monolayer step edge (marked on lower inset image), in comparison with that from a surface far from step edge (mark on the upper inset image).
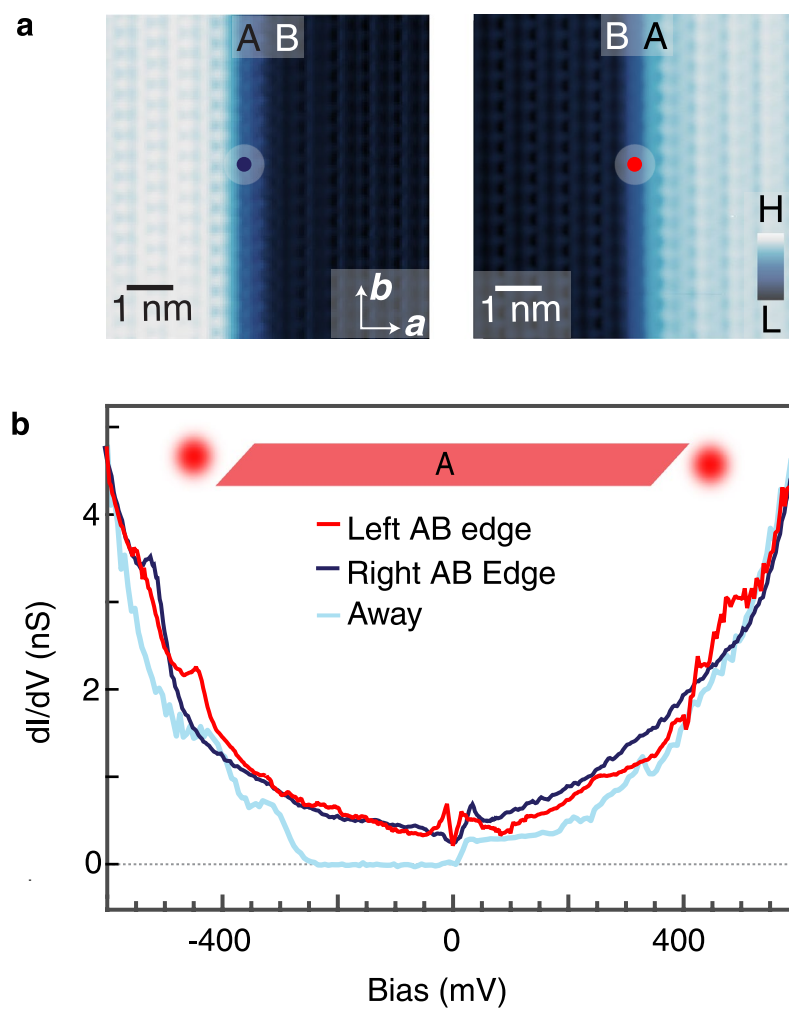
Extended Data Fig. 5 | Tunnelling spectroscopy for both edges of a monolayer step. a, Topographic image of right and left monolayer step edges (AB type). **b**, Differential spectra taken at the left AB monolayer step edge (red), at the right AB monolayer step edge (violet), and away from the edges (blue) reveal the presence of gapless edge states in both AB edges. The inset shows the schematic of the monolayer step edge states.
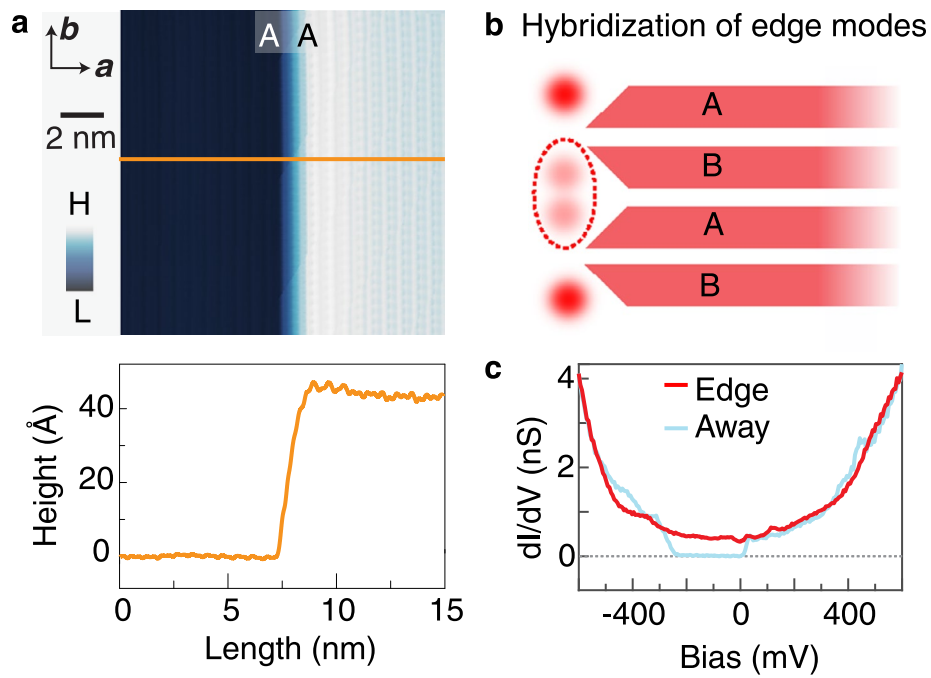
Extended Data Fig. 6 | Hinge state candidate for a four-layer step edge. a. Topographic image and corresponding height profile of a four-layer step edge. **b**, Schematic of a four-layer edge showing quantum hybridization of the quantum spin Hall edge states for neighboring layers. The destructive hybridization is illustrated by the lighter color of the edge states (red spheres). c, Differential spectra taken at the step edge (red) and away from the edge (blue) providing evidence for a candidate gapless hinge state.
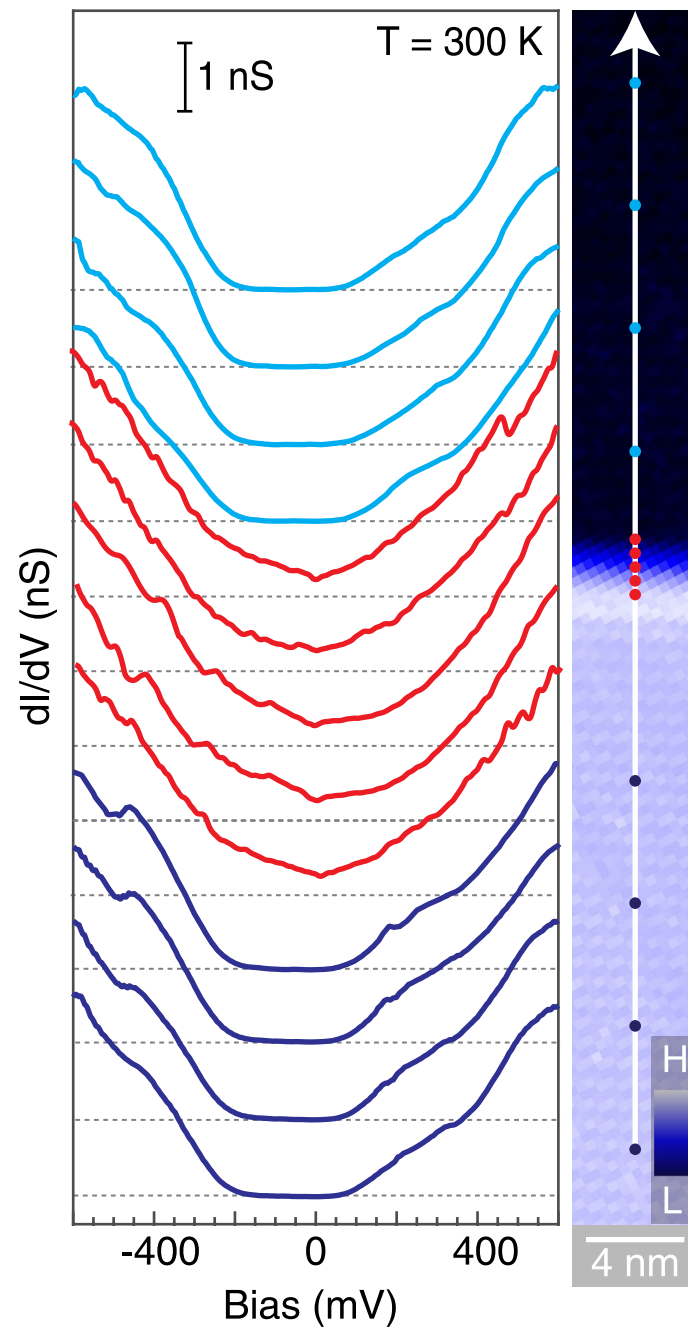
Extended Data Fig. 7 | Spectroscopy of the monolayer edge state at room temperature. Differential spectra of the edge (red curves) and surface (dark and light blue curves), taken along the *a*-axis direction (marked on the corresponding topographic image in the right panel with a white line), exhibit an insulating gap away from edge and gapless edge state at T = 300 K. Spectra are offset for clarity, and their real-space locations are marked on the topography with color-coded dots. Dashed horizontal lines indicate zero density of states of the corresponding spectra.
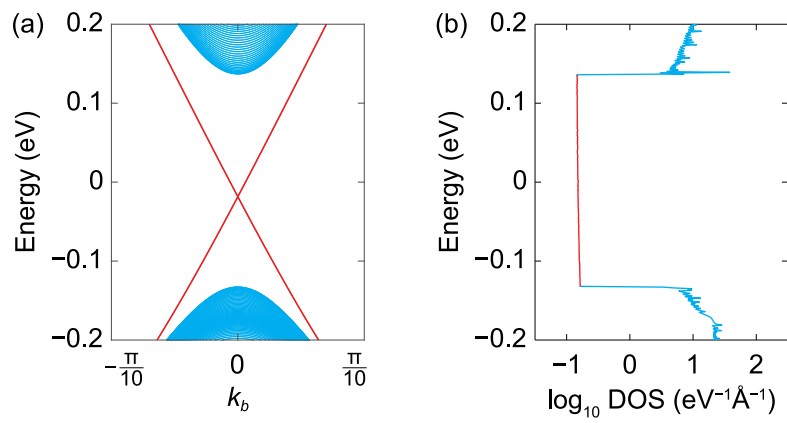
Extended Data Fig. 8 | Calculated helical edge state at a one-layer step edge. a, The edge-projected band structure for a (001) monolayer ribbon on the top surface of Bi_4Br_4. The cyan bands are from the bulk and (001) surfaces of the system. The red bands are the helical edge states. Due to the inversion symmetry of the monolayer, the bands are doubly degenerate at each k_b. The ribbon is infinitely long in the b direction and 200-chain wide in the a direction. **b,** The DOS plotted in a log scale corresponding to the band structure in a.
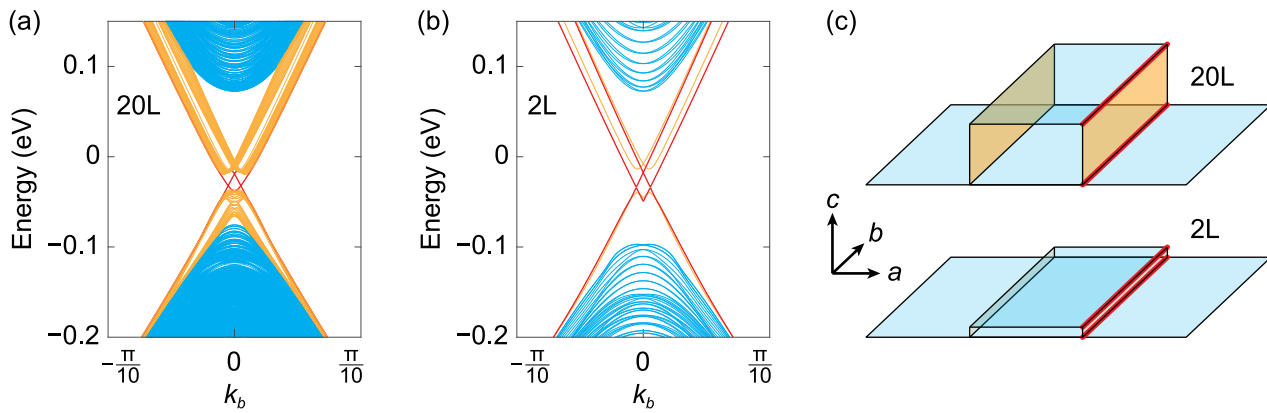
Extended Data Fig. 9 | Calculated bilayer and twenty-layer step-edge states. a, The edge-projected band structure for a (001) twenty-layer ribbon on the top surface of Bi_4Br_4. The cyan bands are from the bulk and (001) surfaces of the system. The orange bands are from the (100) and (-100) side surfaces of the ribbon. The red bands are the gapless hinge states. Due to the inversion asymmetry of even-layer systems, the bands are singly degenerate at each k_b. The ribbon is infinitely long in the b direction and 50-chain wide in the a direction. b, The same as a but for a bilayer ribbon. The two helical edge states from the two monolayers are gapped at one side (orange) but remain almost gapless at the other side (red). c, The real space schematics of the surface and hinge/edge states in a and b.
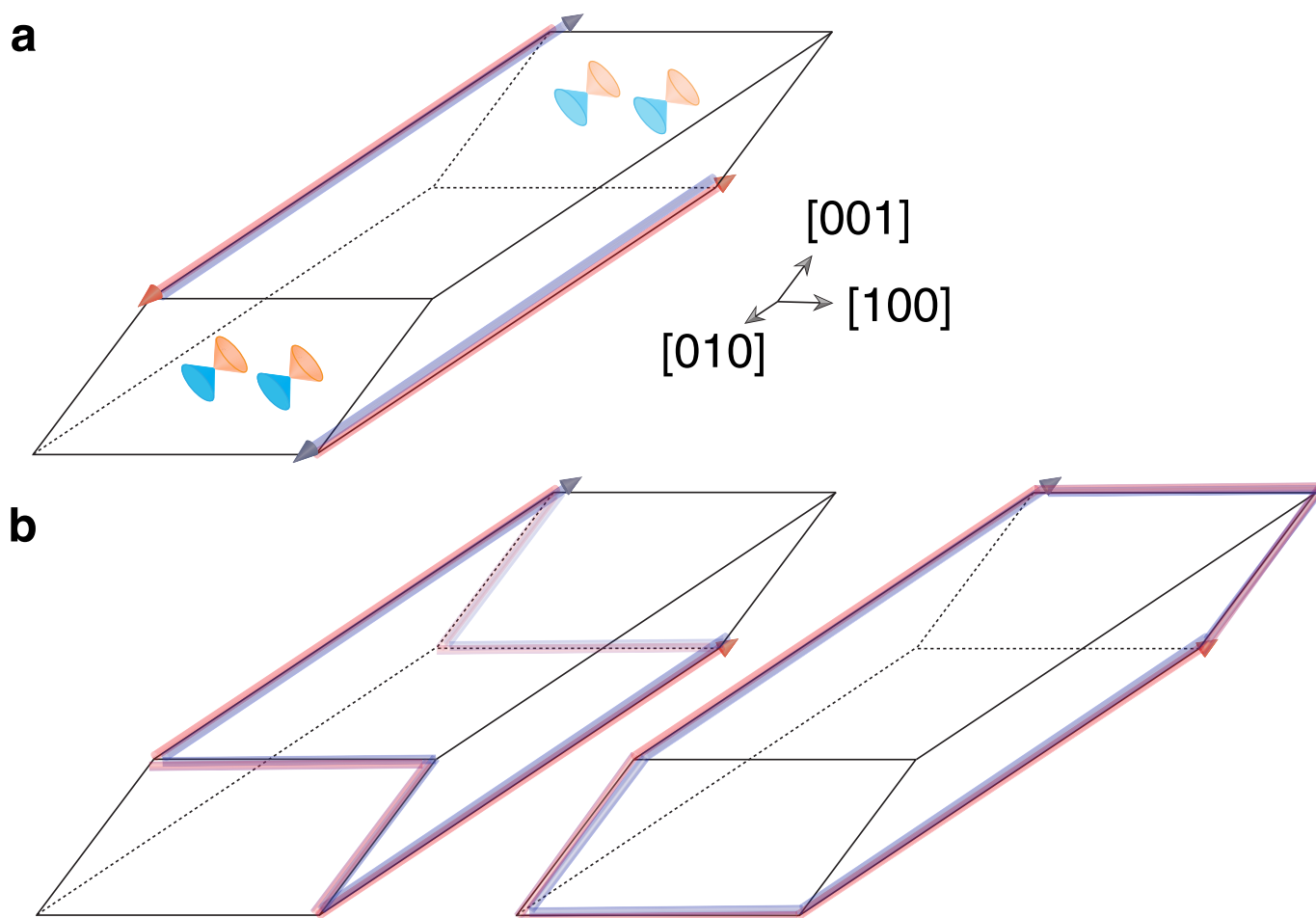
Extended Data Fig. 10 | Topologically protected boundary states in a nanorod geometry with inversion symmetry and C$_2$ rotation symmetry around the [010] axis. a, The nanorod of Bi$_4$Br$_4$ featuring helical hinge states from higher-order band topology and two surface Dirac cones on the (010) surface protected by the C$_2$ rotation symmetry. b, Two possible inversion symmetric paths for the helical hinge states when the C$_2$ symmetry is broken on the (010) surface.